

École doctorale n° 364 : Sciences Fondamentales et Appliquées

Doctorat ParisTech

T H È S E

pour obtenir le grade de docteur délivré par

l'École Nationale Supérieure des Mines de Paris

Spécialité doctorale "Science et Génie des Matériaux"

présentée et soutenue publiquement par

Ali SAAD

le 09 février 2016

NUMERICAL MODELLING OF MACROSEGREGATION FORMED DURING SOLIDIFICATION WITH SHRINKAGE USING A LEVEL SET APPROACH

Co-directeur de thèse: **Charles-André GANDIN**

Co-directeur de thèse: **Michel BELLET**

Jury

Pr. Hervé COMBEAU,	Professeur, Ecole des Mines de Nancy, France	
Pr. Markus RETTENMAYR,	Professeur, Université de Jena, Allemagne	
Pr. Florian KARGL,	Professeur, Agence Spatiale Allemande (DLR), Allemagne	
Dr. Charles-André GANDIN,	Directeur de recherche, CNRS, France	Examineur
Pr. Michel BELLET,	Professeur MINES ParisTech, France	Examineur
Dr. Frédéric COSTES,	Chef de service <i>THERCAST</i> ®, TRANSVALOR S.A., France	Invité

MINES ParisTech

Centre de Mise en Forme des Matériaux (CEMEF)

UMR CNRS 7635, F-06904 Sophia Antipolis, France

Acknowledgement

Dedicated to humanity ...

Contents

1	General Introduction	1
1.1	Solidification notions	2
1.1.1	Solute partitioning	2
1.1.2	Dendritic growth	4
1.1.3	Mush permeability	6
1.2	Macrosegregation	7
1.2.1	Liquid thermosolutal convection	8
1.2.2	Solidification shrinkage	9
1.2.3	Movement of equiaxed grains	9
1.2.4	Solid deformation	9
1.3	Other defects	9
1.4	Industrial Worries	11
1.5	Project context and objectives	12
1.5.1	Context	12
1.5.2	Ojectives and outline	14
2	Modelling Review	19
2.1	Modelling macrosegregation	20
2.1.1	Macroscopic solidification model: monodomain	21
2.2	Eulerian and Lagrangian motion description	27
2.2.1	Overview	27
2.2.2	Interface capturing	30
2.3	Solidification models with level set	30
2.4	The level set method	31
2.4.1	Diffuse interface	32
2.4.2	Mixing Laws	34
2.5	Interface motion	35
2.5.1	Level set transport	36

Contents

2.5.2	Level set regularisation	37
2.6	Mesh adaptation	41
2.6.1	Metrics and anisotropy	41
2.6.2	<i>Remesh2</i> : Interface remeshing	43
2.6.3	<i>Remesh4</i> : Multi-criteria remeshing	44
3	Energy balance with thermodynamic tabulations	47
3.1	State of the art	48
3.2	Thermodynamic considerations	49
3.2.1	Volume averaging	49
3.2.2	The temperature-enthalpy relationship	50
3.2.3	Tabulation of properties	50
3.3	Numerical method	52
3.3.1	Enthalpy-based approach	56
3.3.2	Temperature-based approach	56
3.3.3	Convergence	57
3.4	Validation	58
3.5	Application: multicomponent alloy solidification	61
3.5.1	Tabulations	63
3.5.2	Discussion	65
3.6	Limitations	70
4	Macrosegregation with liquid metal motion	73
4.1	Introduction	75
4.2	Formulation stability	75
4.2.1	Stable mixed finite elements	76
4.2.2	Variational multiscale (VMS)	76
4.3	Navier-Stokes solver	77
4.3.1	Strong and weak formulations	77
4.3.2	Stabilisation parameters	81
4.3.3	Implementation	82
4.4	Application to multicomponent alloys	83
4.4.1	<i>Tsolver</i> validation with fluid flow	83
4.4.2	Results	86
4.5	Macroscopic prediction of channel segregates	92
4.5.1	Introduction	92
4.5.2	Experimental work	93
4.5.3	Macroscopic scale simulations	93

4.6	Meso-Macro prediction of channel segregates	102
4.6.1	Numerical method	102
4.6.2	Configuration	103
4.6.3	Effect of vertical temperature gradient	107
4.6.4	Effect of cooling rate	109
4.6.5	Effect of lateral temperature gradient	111
4.6.6	Mono-grain freckles	112
5	Macrosegregation with solidification shrinkage	115
5.1	Solidification shrinkage	117
5.2	Choice of boundary tracking	117
5.3	Multidomain formalism	119
5.3.1	Assumptions	120
5.3.2	Air-Metal boundary definition	122
5.4	FE partitioned model	123
5.4.1	In the metal	123
5.4.2	In the air	128
5.5	FE monolithic model	130
5.5.1	Monolithic equations	130
5.6	1D application: solidification with inverse segregation	135
5.6.1	Geometry and boundary conditions	135
5.6.2	Shrinkage without macrosegregation	135
5.6.3	Shrinkage with macrosegregation	143
5.7	2D application: controlled solidification benchmark	155
5.7.1	Boundary condition effect	155
5.7.2	Computational configuration	157
5.7.3	Results	158
5.8	3D application: reduced-gravity solidification	163
5.8.1	Previous work	163
5.8.2	Computational configuration	166
5.8.3	Texas binary alloy	173
5.8.4	Texas ternary and quaternary alloys	178
	Bibliography	189

Contents

List of Acronyms

Acronym	Standing for
ALE	Arbitrary Lagrangian-Eulerian
BTR	Brittle temperature range
CAFD	Cellular Automata Finite Difference
CAFE	Cellular Automata Finite Element
CBB	Circumventing Babuška-Brezzi
CCEMLCC	Chill Cooling for the Electro-Magnetic Levitator in relation with Continuous Casting of steel
CEMEF	Centre de Mise en Forme des Matériaux
CFL	Courant–Friedrichs–Lewy
C.FL.	Computing and FLuids
CSF	Continuum Surface Force
DLR	Deutsches Zentrum für Luft- und Raumfahrt
DSPG	Darcy-Stabilising/Petrov-Galerkin
EML	Electromagnetic levitation
ESA	European Space Agency
FEM	Finite Element Method
FVM	Finite Volume Method
GMAW	Gas Metal Arc Welding
ISS	International Space Station
IWT	Institut für Werkstofftechnik
LHS	Left-hand side
LSIC	Least squares on incompressibility constraint
LSM	Level set method
MAC	Marker-and-cell
PF	Phase field
PSPG	Pressure-Stabilising/Petrov-Galerkin
RHS	Right-hand side
RUB	Ruhr Universität Bochum
RVE	Representative Elementary Volume
SBB	Satisfying Babuška-Brezzi
SUPG	Streamline-Upwind/Petrov-Galerkin
VMS	Variational MultiScale
VOF	Volume Of Fluid

Contents

Chapter 3

Energy balance with thermodynamic tabulations

Contents

3.1 State of the art	48
3.2 Thermodynamic considerations	49
3.2.1 Volume averaging	49
3.2.2 The temperature-enthalpy relationship	50
3.2.3 Tabulation of properties	50
3.3 Numerical method	52
3.3.1 Enthalpy-based approach	56
3.3.2 Temperature-based approach	56
3.3.3 Convergence	57
3.4 Validation	58
3.5 Application: multicomponent alloy solidification	61
3.5.1 Tabulations	63
3.5.2 Discussion	65
3.6 Limitations	70

3.1 State of the art

To model macrosegregation during solidification, a minimum of four conservation equations are necessary: conservation of mass, momentum, chemical species and energy. The phase change literature contains a wealth of numerical methods to solve energy conservation in solidifying alloys. A comprehensive overview of these methods is given by [Swaminathan and Voller \[1993\]](#).

The corresponding equation associates the total average enthalpy to the temperature via intrinsic alloy properties, such as the heat capacity of the phases and the latent heat associated with the phase transformations. However, in the course of solidification and while macrosegregation is taking place, these properties change because the average composition may vary significantly: the transformation paths are thus modified, as well as the phases' composition and heat capacity. Similarly, the latent heat of phase transformations is not a mere constant that could be distributed as a function of the phase fractions assuming only temperature-dependent phases' properties, as often found in the literature [[Bellet et al. 2009](#)]. It is thus impossible to establish a priori the dependence of the enthalpy with respect to temperature when macrosegregation alters the average composition, even in the case of full thermodynamic equilibrium between phases.

In this chapter, we discuss a suitable numerical scheme based on an enthalpy method, already used in the literature to alleviate this macrosegregation-related problem [[Swaminathan and Voller 1993](#); [Carozzani et al. 2013](#)]. Later on, we introduce a modified formulation, using the effective heat capacity method that increases the original scheme's efficiency.

This chapter introduces an enthalpy method that makes use of a temperature-based solver. It uses tabulated thermodynamic quantities (solidification paths, phases' enthalpy and composition) in a range of average compositions and temperatures as found in the literature [[Doré et al. 2000](#); [Thuinet and Combeau 2004](#); [Du et al. 2007](#)], with the aim of evaluating the total average enthalpy as well as the effective heat capacity. The novelty of the modified method resides in the use of thermodynamic tabulations without losing the advantages of the previous method, thus yielding faster computation times while maintaining a good accuracy.

3.2 Thermodynamic considerations

3.2.1 Volume averaging

The volume averaging technique, presented in [section 2.1.1](#), is considered when solving the energy equation in the presence of macrosegregation. The reason is that phase properties and distributions varying with the average composition, have a great impact on the average thermal properties, and hence on the overall heat transfer in the system. We recall the basic expression of the volume averaged value of a field ψ , by writing:

$$\langle \psi \rangle = \sum_{\phi} g^{\phi} \langle \psi \rangle^{\phi} \quad (3.1)$$

where g^{ϕ} denotes the volume fraction of phase ϕ in the RVE, and $\langle \psi \rangle^{\phi}$ is the intrinsic average of the quantity ψ in the RVE. It should be emphasized that the averaging technique applies to virtually all thermodynamic volumetric variables (enthalpy, density ...). Among these variables, the temperature is also considered to be uniform in the RVE.

Applying the volume averaging technique to the energy conservation equation along with interfacial balances between the phases, results in the following averaged equation [[Rappaz et al. 2003](#)]:

$$\frac{\partial \langle \rho h \rangle}{\partial t} + \nabla \cdot \langle \rho h \mathbf{v} \rangle = \nabla \cdot (\langle \kappa \rangle \nabla T) + \langle \dot{Q}_V \rangle \quad (3.2)$$

where ρ stands for the density, h the mass enthalpy, \mathbf{v} the velocity field, κ the thermal conductivity, T the temperature and \dot{Q}_V a possible volumetric heat source. [Equation \(3.2\)](#) is the standard averaged form of the energy conservation equation used in non-stationary phase change problems.

It is clear that the nature of the temperature-enthalpy relationship plays a central role when formulating the resolution strategy of this nonlinear equation. Generally, it is admitted that, depending on the resolution strategy, it is necessary to express enthalpy as a function of temperature or vice-versa, together with associated partial derivatives, $\frac{\partial \langle \rho h \rangle}{\partial T}$ or $\frac{\partial T}{\partial \langle \rho h \rangle}$.

It is noted that in the FEM context, the RVE is represented by a node in a finite element, so for instance the temperature in a RVE is denoted T_j henceforth, where j represents the index of the node localising the RVE.

3.2.2 The temperature-enthalpy relationship

In solidification problems, additional variables are involved in [eq. \(3.1\)](#) and [eq. \(3.2\)](#), like the transformation path that defines the history of the phase fractions, as well as the average chemical composition $\langle w_i \rangle$, i being the index of the chemical species (only the solutes are considered). The temperature-enthalpy relation averaged over the phases in a given RVE writes:

$$\langle \rho h \rangle = \sum_{\phi} g^{\phi}_{(T, \langle w_i \rangle \dots)} \langle \rho \rangle^{\phi}_{(T, \langle w_i \rangle \dots)} \langle h \rangle^{\phi}_{(T, \langle w_i \rangle \dots)} \quad (3.3)$$

Note that the volume average enthalpy is approximated by the product $\langle \rho h \rangle^{\phi} = \langle h \rangle^{\phi} \langle \rho \rangle^{\phi}$ in the current work. As stated in the introduction, it becomes clear from [eq. \(3.3\)](#) that phase properties, i.e. average phase density, $\langle \rho \rangle^{\phi}$ and enthalpy, $\langle h \rangle^{\phi}$, are temperature and composition dependent. This equation is the key to convert the average volume enthalpy to temperature (through a procedure named *H2T*) or vice-versa (*T2H*). The values of the different phase fractions g^{ϕ} (solidification path) and phase enthalpies $\langle \rho h \rangle^{\phi}$ are thus needed to close the relation.

3.2.3 Tabulation of properties

The complexity of performing a thermodynamic conversion is directly linked to the simplicity of determining the alloy properties, namely the phase fractions and both phase densities and enthalpies. In the case of binary alloys and with several assumptions with respect to the system (e.g., linear monovariant lines in temperature-composition relationships of the phase diagram, constant heat capacity of phases and constant latent heat of transformations, equilibrium approximations between phases) analytical calculations are often used to determine the phase fractions and phase compositions. Nevertheless, analytical relations are more complex or even impossible to derive in the case of multicomponent alloys ($i > 1$), or even for binary alloys with multiple phase transformations (e.g. peritectic and eutectic reactions) with a nonlinear phase diagram.

To overcome this problem, one can resort to thermodynamic databases and phase equilibrium calculations to tabulate the transformation paths and the phase densities and enthalpies for a given range of temperatures and average compositions. It is a handy solution for two main reasons: first, the conversion is merely a binary search in a table; secondly, it is a simple solution for coupling with macrosegregation. In this way, phase fractions g^{ϕ} are tabulated as functions of temperature and average composition, while for each phase ϕ the mass enthalpy, $\langle h \rangle^{\phi}$, and the density, $\langle \rho \rangle^{\phi}$, are

tabulated as functions of temperature and phase intrinsic average compositions $\langle w_i \rangle^\phi$, as well as other possible parameters.

Table 3.1 summarizes the steps in order to perform a temperature-to-enthalpy ($T2H$) conversion using the predefined tabulation approach. In step 1, the transformation path is acquired for each average composition, $\langle w_i \rangle$, and temperature, T , to determine the list of phases, their volume fractions g^ϕ and their intrinsic compositions $\langle w_i \rangle^\phi$, assuming full equilibrium. In step 2, the phase enthalpy $\langle h \rangle^\phi$ and density $\langle \rho \rangle^\phi$ are determined by searching for the temperature and the already known phase composition $\langle w_i \rangle^\phi$. In step 3, the average volume enthalpy is computed from the volume fraction, density and mass enthalpy of phases using [eq. \(3.3\)](#). A flowchart explaining $T2H$ conversion steps is given in [fig. 3.1](#).

Table 3.1 – Tabulation processing for a $T2H$ procedure

Step Number	1	2	3
Inputs	$T, \langle w_i \rangle$	$T, \langle w_i \rangle^\phi$	$g^\phi, \langle \rho \rangle^\phi, \langle h \rangle^\phi$
Outputs	$g^\phi, \langle w_i \rangle^\phi$	$\langle \rho \rangle^\phi, \langle h \rangle^\phi$	$\langle \rho h \rangle$ (eq. (3.3))

The methodology to build the tabulations is straightforward. It is based on two main scans. On the one hand, intervals for the variation of the average composition $\langle w_i \rangle$ are chosen from the known alloy composition. These variations have to cover the extreme values adopted during the simulation, which are not known a priori. An interval is also selected for the variation of temperature. The latter is easier to determine as it usually starts from the initial melt temperature and goes down to the room temperature in a standard casting simulation. For each mapping of composition and temperature, a thermodynamic equilibrium state is computed. The outputs are the number of phases encountered, together with their fraction and intrinsic compositions. On the other hand, for each phase, a scan of the intrinsic composition and temperature is made to compute the intrinsic properties. The same temperature interval and step as defined earlier are used.

Regarding the enthalpy-to-temperature conversion ($H2T$) shown in the flowchart in [fig. 3.2](#), a backward iterative $T2H$ search is performed. For a known composition $\langle w_i \rangle$, denoting (τ) the iteration index to convert the enthalpy H_{input} , we start with an initial guess for temperature $T^{(\tau=0)}$ then convert it to an enthalpy $H^{(\tau=0)}$ with the $T2H$ conversion. Using an appropriate nonlinear algorithm (Brent is the most versatile in our case), we aim at minimizing the following scalar residual: $R_H = |H_{\text{input}} - H^{(\tau)}|$. Once the algorithm has converged, the temperature $T^{(\tau)}$ is the result of the $H2T$ conversion. It is inferred that the first conversion ($T2H$) is a direct one whereas the latter ($H2T$) is

indirect and requires a series of iterative steps; each step being a single $T2H$ resolution. In other words, a $H2T$ conversion is a backward search for a temperature, hence it is slower. It is important to realise that this conversion's speed lag is exacerbated when tabulations increase in size (e.g. large number of temperature and composition steps) and complexity (e.g., multicomponent industrial alloys used in casting), since the search gets more complicated with the increasing number of input columns (one column for each alloying element).

Initialisation	
Temperature	T_j
Average composition	$\langle w_i \rangle_j$
Microsegregation law	
Phase fractions	$(T_j, \langle w_i \rangle_j) \rightarrow g_j^\phi$
Phase compositions	$(T_j, \langle w_i \rangle_j) \rightarrow \langle w_i \rangle_j^\phi$
Phase mass enthalpies	$(T_j, \langle w_i \rangle_j^\phi) \rightarrow \langle h \rangle_j^\phi$
Phase densities	$(T_j, \langle w_i \rangle_j^\phi) \rightarrow \langle \rho \rangle_j^\phi$
Total enthalpy	
$\langle \rho h \rangle_j = \sum_\phi \left[g_j^\phi \langle \rho \rangle_j^\phi \langle h \rangle_j^\phi \right]_{T_j}$ (eq. (3.3))	

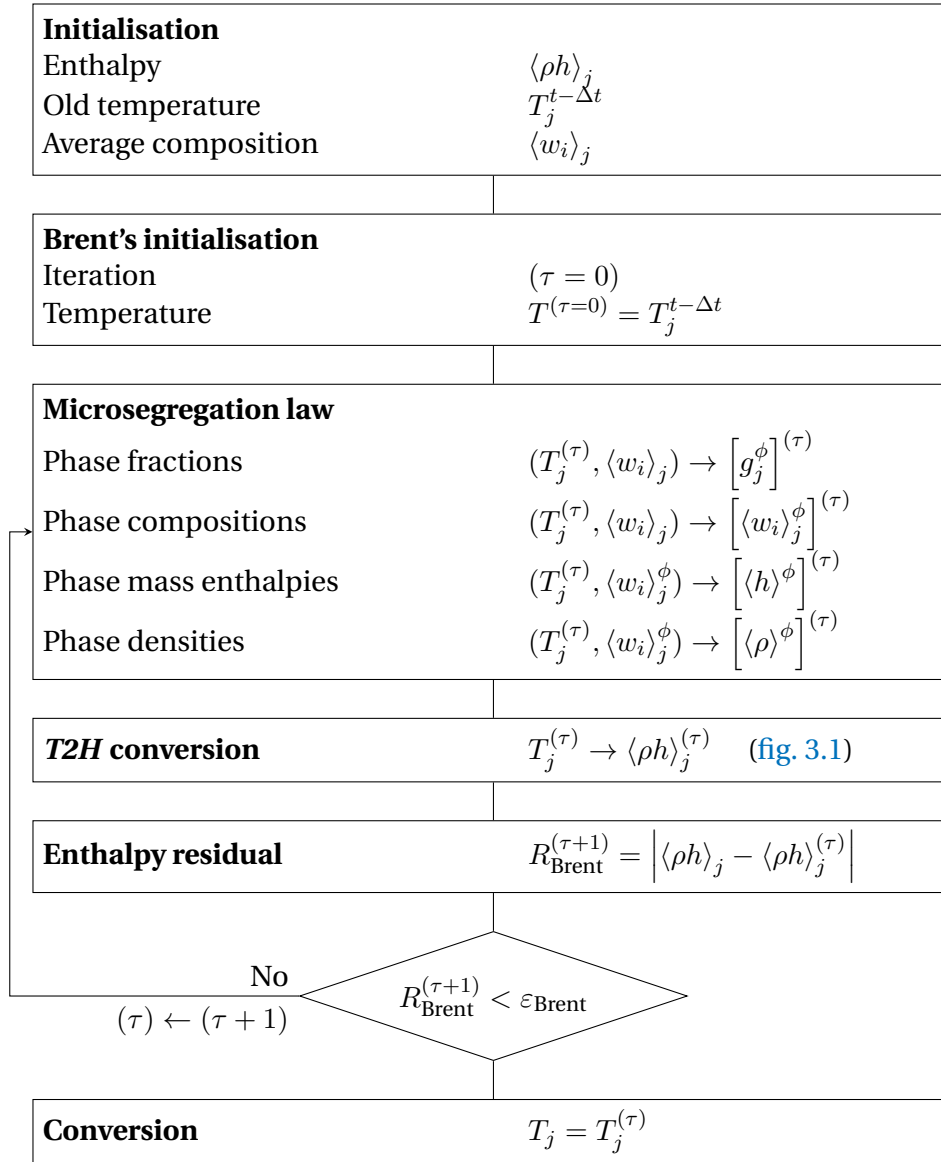
Fig. 3.1 – Algorithm for a single temperature to enthalpy ($T2H$) conversion at node j .

3.3 Numerical method

The finite element method is used to solve the energy conservation as expressed by eq. (3.2). A test function \mathcal{W} belonging to the Hilbertian Sobolev space $\mathcal{H}^1(\Omega_E)$ of continuous integrable test functions is used to formulate the integral variational form of eq. (3.2) [Süli 2000]. A Fourier boundary condition is considered on the domain boundary $\partial\Omega_E$. The domain Ω is discretised using first-order linear simplexes, Ω_E , defined by their number of local nodes, NbLoc: triangles in 2D with NbLoc=3 and tetrahedra in 3D with NbLoc=4. The outcome is a residual that we aim to minimize so that the conservation principle is satisfied. Therefore, the weak form writes:

$$\forall \mathcal{W} \in M = \{u \in \mathcal{H}^1(\Omega_E)\}$$

$$\int_{\Omega_E} \mathcal{W} \frac{\partial H}{\partial t} dV + \int_{\Omega_E} \mathcal{W} \langle \mathbf{v}^l \rangle \cdot \nabla \langle \rho h \rangle^l dV - \int_{\Omega_E} \mathcal{W} \nabla \cdot (\langle \kappa \rangle \nabla T) dV - \int_{\Omega_E} \mathcal{W} \langle \dot{Q}_V \rangle dV = 0$$
(3.4)


 Fig. 3.2 – Algorithm for a single enthalpy to temperature (H2T) conversion at node j .

Chapter 3. Energy balance with thermodynamic tabulations

where $H = \rho h$ is the average volumetric enthalpy, introduced to simplify notations in the following. Furthermore, we assume a static solid phase and an incompressible liquid phase, which allows recasting the second term of eq. (3.2) into $\langle \mathbf{v}^l \rangle \cdot \nabla \langle \rho h \rangle^l$. $\langle \rho h \rangle^l = \langle \rho \rangle^l \langle h \rangle^l$ is not main variable of the energy conservation equation's weak form, eq. (3.4). Therefore we express it as a function of temperature, which is related to the main variable via the enthalpy-temperature relation:

$$\nabla \langle \rho h \rangle^l = \nabla \left(\langle \rho \rangle^l \langle h \rangle^l \right) = \langle \rho \rangle^l C_p^l \nabla T \quad (3.5)$$

where C_p^l is the mass heat capacity of the liquid phase. Ideally, this value should be taken directly from the thermodynamic database if it is available. Otherwise, it can be derived by differentiation of the tabulated liquid mass enthalpy with respect to temperature. In this work, C_p^l is considered constant, equal to the alloy's initial mass heat capacity. The steps for discretising in time and space eq. (3.4) are well detailed in some text books like Rappaz et al. [2003]. As for enthalpy and temperature, they are spatially discretised in each simplex using interpolations functions \mathcal{P} , thus defining the nodal values H_j and T_j , respectively:

$$H = \sum_{j=1}^{\text{NbLoc}} \mathcal{P}_j H_j \quad (3.6)$$

$$T = \sum_{j=1}^{\text{NbLoc}} \mathcal{P}_j T_j \quad (3.7)$$

The Galerkin formulation gives the expression for the residual contribution at a mesh node i (here i is not the usual solute index) for time step t in a local element Ω_E :

$$\begin{aligned} (R_i^E)^t &= \mathcal{M}_{ij}^E \left(H_j^t - H_j^{t-\Delta t} \right) + \mathcal{A}_{ij}^E T_j^t + (\mathcal{K}1_{ij}^E + \mathcal{K}2_{ij}^E) T_j^t - \mathcal{F}_i^E - \mathcal{Q}_i^E = 0 \\ i, j &: 1 \rightarrow \text{NbLoc} \end{aligned} \quad (3.8)$$

where the volumetric contributions are detailed as follows:

$$\text{transient term: } \mathcal{M}_{ij}^E = \int_{\Omega_E} \frac{1}{\Delta t} \mathcal{P}_i \mathcal{P}_j \, dV \quad (3.9)$$

$$\text{advection term: } \mathcal{A}_{ij}^E = \int_{\Omega_E} \langle \rho \rangle^l C_p^l \mathcal{P}_i \langle \mathbf{v}^l \rangle \cdot \nabla \mathcal{P}_j \, dV \quad (3.10)$$

$$\text{diffusion term: } \mathcal{K}1_{ij}^E = \int_{\Omega_E} \langle \kappa \rangle \nabla \mathcal{P}_i \nabla \mathcal{P}_j \, dV \quad (3.11)$$

$$\text{source term: } \mathcal{Q}_i^E = \int_{\Omega_E} \mathcal{P}_i \langle \dot{Q}_V \rangle \, dV \quad (3.12)$$

while the surface boundary contributions are given by:

$$\text{boundary condition term 1: } \mathcal{K}2_{ij}^E = \int_{\partial\Omega_E} h_{\text{ext}} \mathcal{P}_i \mathcal{P}_j \, dS \quad (3.13)$$

$$\text{boundary condition term 2: } \mathcal{F}_i^E = \int_{\partial\Omega_E} h_{\text{ext}} T_{\text{ext}} \mathcal{P}_i \, dS \quad (3.14)$$

$$(3.15)$$

The surface integrals $\mathcal{K}2_{ij}^E$ and \mathcal{F}_i^E are related to a Fourier-type boundary condition, with h_{ext} as a coefficient of heat exchange and T_{ext} as the external temperature far from the boundary. The energy conservation principle is satisfied when the sum of the residual contributions coming from all the mesh elements is zero. In other words, the following global residual defined by the assembly of these contributions, should be minimized:

$$(R_i)^t = \mathcal{M}_{ij} \left(H_j^t - H_j^{t-\Delta t} \right) + \mathcal{A}_{ij} T_j^t + (\mathcal{K}1_{ij} + \mathcal{K}2_{ij}) T_j^t - \mathcal{F}_i - \mathcal{Q}_i = 0 \quad (3.16)$$

$i, j : 1 \rightarrow \text{NbGlob}$

where the global tensors \mathcal{M}_{ij} , \mathcal{A}_{ij} , $\mathcal{K}1_{ij}$, $\mathcal{K}2_{ij}$, \mathcal{F}_i and \mathcal{Q}_i contain respectively, after an assembly step, the contributions of the local matrices \mathcal{M}_{ij}^E , \mathcal{A}_{ij}^E , $\mathcal{K}1_{ij}^E$, $\mathcal{K}2_{ij}^E$, \mathcal{F}_i^E and \mathcal{Q}_i^E from each discretised element in the domain Ω . Accordingly, the indices i and j refer to global node numbers, where the total number of nodes is denoted by "NbGlob".

It is clear that the global residual inherits the dependence between volumetric enthalpy and temperature. This is shown in [eq. \(3.16\)](#) where the average volume enthalpy is a function of the temperature. It infers that this residual is a non-linear function; therefore minimizing it requires an iterative non-linear algorithm.

Our choice settles on the Newton-Raphson method, known for its quadratic convergence speed. A solidification problem can induce severe non-linearities from the release of the latent heat (which itself is temperature and composition dependent) and the variations of the average thermophysical properties of the alloy with respect to temperature, phase fraction and average composition. This algorithm could thus treat such variations. Considering the link between the properties and temperature, [eq. \(3.16\)](#) may be solved either for the average volumetric enthalpy or for the temperature as the nodal unknown, hence both formulations are presented hereafter.

3.3.1 Enthalpy-based approach

The residual is re-written using a Taylor series expansion to the first order for a non-linear iteration $(\nu - 1)$:

$$(R_i)^{(\nu)} = (R_i)^{(\nu-1)} + \left(\frac{\partial R}{\partial H} \right)_{ij}^{(\nu-1)} \Delta H_j^{(\nu-1)} + \mathcal{O}(H_j^2) \quad (3.17)$$

Neglecting the second order terms, the suggested correction at each iteration in view of cancelling the residual and giving the new value $H_j^{(\nu-1)}$, is given by the linear system in [eq. \(3.18\)](#) relative to what we call the *Hsolver*:

$$\left(\frac{\partial R}{\partial H} \right)_{ij}^{(\nu-1)} \left(H_j^{(\nu)} - H_j^{(\nu-1)} \right) = -R_i^{(\nu-1)} \quad (3.18)$$

where $\overline{\frac{\partial R}{\partial H}}$ is a global tangent matrix yielding the variations of the residual vector $\mathbf{R}^{(\nu-1)}$ with respect to the volumetric enthalpy vector in the previous iteration, $\mathbf{H}^{(\nu-1)}$. The detailed flow chart for the *Hsolver* is given in [fig. 3.3](#). If [eq. \(3.8\)](#) is considered, then the contribution of an element Ω_E writes:

$$\left(\frac{\partial R^E}{\partial H} \right)_{ij}^{(\nu-1)} = \underbrace{\mathcal{M}_{ij}^E + \mathcal{A}_{ij}^E \left(\frac{\partial T}{\partial H} \right)_j^{(\nu-1)}}_{\text{no sum on } j} + \underbrace{(\mathcal{K}1_{ij}^E + \mathcal{K}2_{ij}^E) \left(\frac{\partial T}{\partial H} \right)_j^{(\nu-1)}}_{\text{no sum on } j} \quad (3.19)$$

[Equation \(3.19\)](#) is the core of the enthalpy-based solver. The resolution of [eq. \(3.18\)](#) then yields a new estimate of the vector of nodal volumetric enthalpies $H^{(\nu)}$, which are the only unknowns to be solved for. Once determined at iteration $(\nu - 1)$, convergence tests are performed.

3.3.2 Temperature-based approach

Similarly to the *Hsolver*, the local residual is recast for a nonlinear iteration $(\nu - 1)$, leading this time to an iterative temperature correction:

$$\left(\frac{\partial R}{\partial T} \right)_{ij}^{(\nu-1)} \left(T_j^{(\nu)} - T_j^{(\nu-1)} \right) = -R_i^{(\nu-1)} \quad (3.20)$$

where $\overline{\frac{\partial R}{\partial T}}$ is a global tangent matrix yielding the variations of the residual with respect to the temperature vector, $\mathbf{T}^{(\nu-1)}$, at the previous iteration. This solver will be referred to as the *Tsolver*. The corresponding flow chart is given in [fig. 3.4](#). The contribution of

an element Ω_E to this tangent matrix is evaluated as:

$$\left(\frac{\partial R^E}{\partial T}\right)_{ij}^{(\nu-1)} = \underbrace{\mathcal{M}_{ij}^E \left(\frac{\partial H}{\partial T}\right)_j^{(\nu-1)}}_{\text{no sum on } j} + \mathcal{A}_{ij}^E + (\mathcal{K}1_{ij}^E + \mathcal{K}2_{ij}^E) \quad (3.21)$$

In contrast to the previous solver, [eq. \(3.21\)](#) is the core of the temperature-based solver. The resolution of [eq. \(3.20\)](#) then yields a new estimate of the vector of nodal temperatures $T^{(\nu)}$, which are the only unknowns to be solved for. Once updated for iteration $(\nu - 1)$, convergence tests are performed.

3.3.3 Convergence

The previous two sections described the iterative resolution of the same discretised energy conservation by both *Tsolver* and *Hsolver*. However, in [eqs. \(3.19\)](#) and [\(3.21\)](#), an important term emerges from the tangent matrix evaluation describing the variations between enthalpy and temperature: $\frac{\partial T}{\partial H}$ and $\frac{\partial H}{\partial T}$.

This term invokes the previously mentioned temperature-enthalpy tabulations which depend on the alloy composition. Consequently, the vector of nodal values $\frac{\partial T}{\partial H}$ (respectively $\frac{\partial H}{\partial T}$) has a great influence on the convergence of the *Hsolver* (respectively the *Tsolver*). When [eq. \(3.18\)](#) or [eq. \(3.20\)](#) is solved at iteration (ν) , this term is written using a finite difference:

$$\textbf{Hsolver} \quad \left(\frac{\partial T}{\partial H}\right)_j^{(\nu)} = \frac{T_j^{(\nu)} - T_j^{(\nu-1)}}{\langle \rho h \rangle_j^{(\nu)} - \langle \rho h \rangle_j^{(\nu-1)}} \quad (3.22)$$

$$\textbf{Tsolver} \quad \left(\frac{\partial H}{\partial T}\right)_j^{(\nu)} = \frac{\langle \rho h \rangle_j^{(\nu)} - \langle \rho h \rangle_j^{(\nu-1)}}{T_j^{(\nu)} - T_j^{(\nu-1)}} \quad (3.23)$$

For the *Tsolver*, the enthalpy vector $H^{(\nu-1)}$ is needed to evaluate [eq. \(3.23\)](#). In contrast, the *Hsolver* requires the values of $T^{(\nu-1)}$ vector to evaluate the corresponding [eq. \(3.22\)](#). In both cases, the unknown is determined by the tabulations. The indices next to the mentioned unknowns indicate that this relation is used for each iteration (ν) at each mesh node j , hence affecting the global resolution time between the two solvers. The *Hsolver* needs a *H2T* to evaluate $\frac{\partial T}{\partial H}$, whereas the *Tsolver* needs a *T2H* to evaluate the vector $\frac{\partial H}{\partial T}$. It can be seen that *Tsolver* uses solely *T2H* procedure (flowchart in [fig. 3.1](#)) and the thermodynamic tabulations to determine the volumetric enthalpy, hence the term $\frac{\partial H}{\partial T}$. On the other hand, *Hsolver* repeats the same procedure a finite number of times in order to determine a temperature output through *H2T*

(flowchart in [fig. 3.2](#)) and use it to compute $\frac{\partial T}{\partial H}$. This algorithmic difference leverages the *Tsolver* in terms of computation time providing the same numerical accuracy while conserving the total system energy.

Convergence tests are necessary at the end of each iteration of the energy solver to determine the convergence status of the algorithm. In the context of the *Tsolver* for instance, the residual is re-evaluated with the newly determined temperature vector $\mathbf{T}^{(\nu)}$ and enthalpy vector $\mathbf{H}^{(\nu)}$ so [eq. \(3.16\)](#) rewrites:

$$(R_i)^{(\nu)} = \mathcal{M}_{ij} \left(H_j^{(\nu)} - H_j^{t-\Delta t} \right) + \mathcal{A}_{ij} T_j^{(\nu)} + (\mathcal{K}1_{ij} + \mathcal{K}2_{ij}) T_j^{(\nu)} - \mathcal{F}_i - \mathcal{Q}_i \quad (3.24)$$

$i, j : 1 \rightarrow \text{NbGlob}$

The norm of the current residual, $\|\mathbf{R}^{(\nu)}\|$, is compared to a fixed small value $\varepsilon_R \approx [10^{-5}; 10^{-4}]$. The resulting temperature variation, $|T_j^{(\nu-1)} - T_j^{(\nu-1)}|$, should also respond to similar criterion between two consecutive iterations. For that purpose, we compare it to another fixed value $\varepsilon_T \approx [10^{-3}; 10^{-2}]$. Convergence is ultimately achieved when the following criteria are simultaneously met:

$$\begin{cases} \|\mathbf{R}^{(\nu)}\| < \varepsilon_R \\ \text{Max}_{j:1 \rightarrow \text{NbGlob}} |T_j^{(\nu)} - T_j^{(\nu-1)}| < \varepsilon_T \end{cases} \quad (3.25)$$

A comparison of both solver formulations is done in the hereafter test cases section.

3.4 Validation

The two solvers are tested in a purely diffusive case for a one-dimensional solidification configuration. Predictions with a 1D front tracking model [[Gandin 2000](#)] are used as a benchmark. They provide solutions for the temperature and solid fraction during directional solidification of a 10 cm long ingot. The nominal composition, w_0 , is Al-7 wt.% Si. The melt having a uniform initial temperature, T_0 , is cooled with a heat exchange coefficient, h_{ext} , with a fixed external temperature, T_{ext} (assuming a Fourier boundary condition) from one side, the other side being adiabatic. The initial conditions, boundary conditions and alloy properties are all listed in [table 3.2](#).

For this simple test case, we use linear temperature dependence of the intrinsic phase enthalpies, that is $\langle \rho h \rangle^s = \rho C_p T$ and $\langle \rho h \rangle^l = \rho(C_p T + L)$, where ρ is the alloy density, C_p is the heat capacity per unit mass and L is the latent heat per unit mass. Values for ρ , C_p and L , as well as for the thermal conductivities, $\kappa = \langle \kappa \rangle^l = \langle \kappa \rangle^s$, are taken constant.

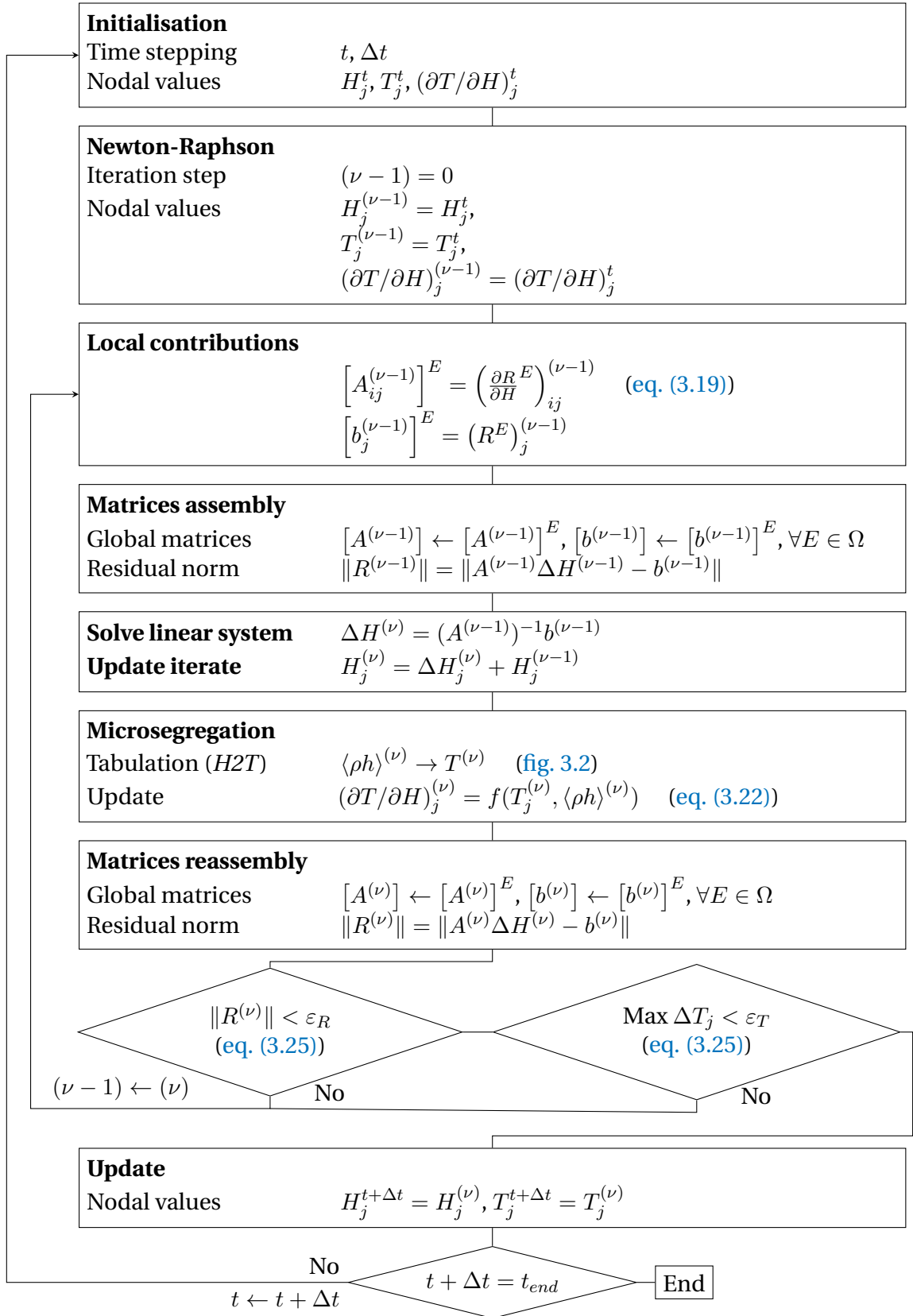


Fig. 3.3 – Resolution algorithm of the enthalpy-based solver.

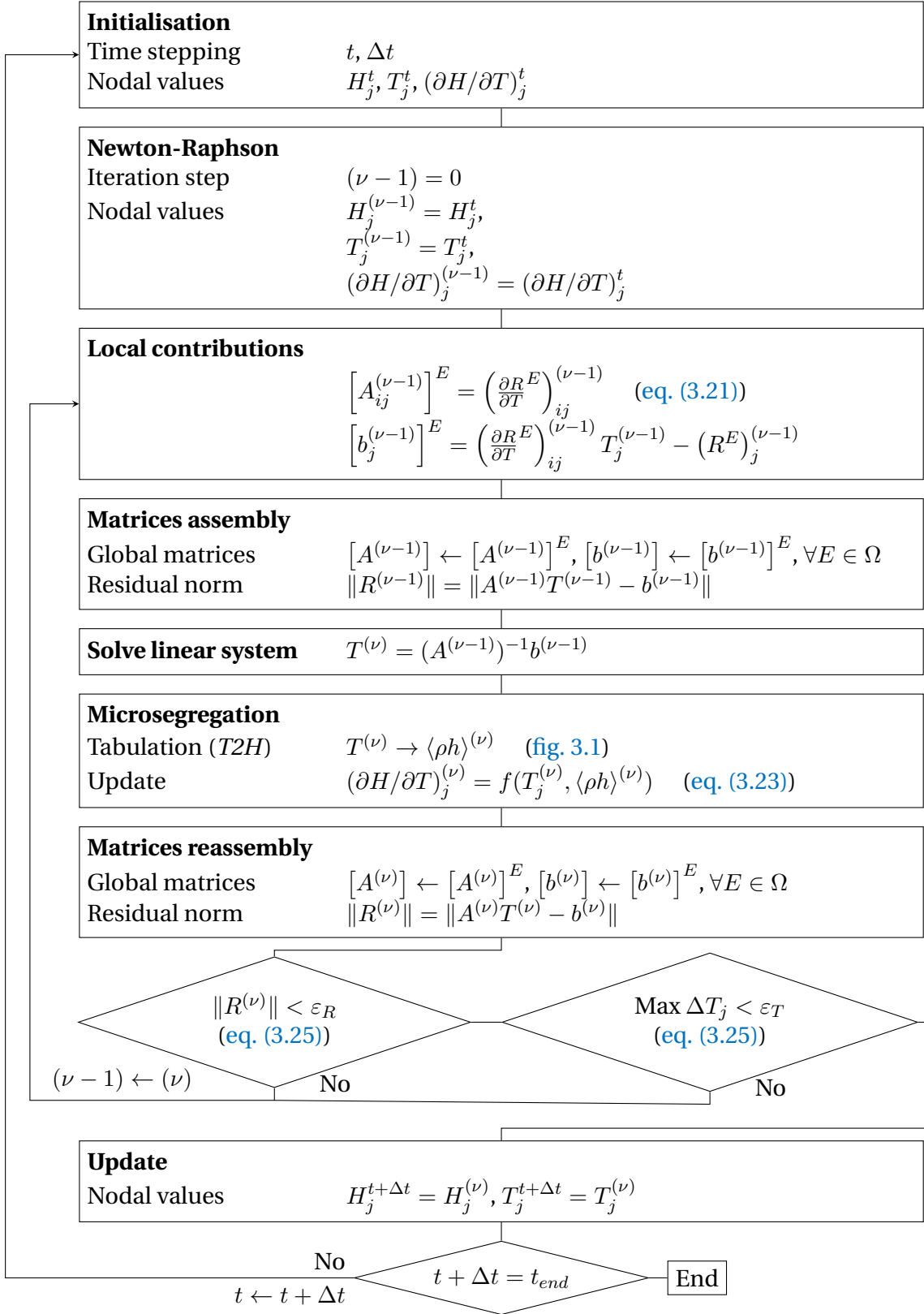


Fig. 3.4 – Resolution algorithm of the temperature-based solver.

3.5. Application: multicomponent alloy solidification

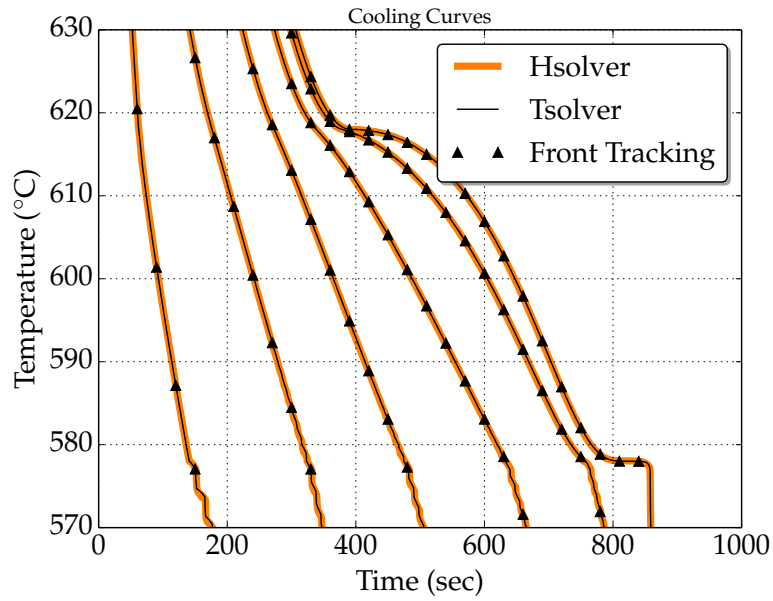
A Gulliver-Scheil approximation is used to compute a single relationship between temperature and volume solid fraction, g^s , in the absence of macrosegregation. This is done assuming a linear binary phase diagram and thus requires using the properties listed in [table 3.2](#), i.e. the segregation coefficient, k , the liquidus slope, m_L , the liquidus temperature, T_L , and the eutectic temperature, T_E . [Figure 3.5](#) shows the comparison with the *Hsolver* and *Tsolver*. The cooling curves and liquid fraction results are found superimposed to the front tacking solution, thus giving validation of the implementation as well as the iterative schemes presented above to solve the energy conservation

Table 3.2 – Parameters for the pure diffusion test case with an Al-7 wt.% Si alloy presented in [fig. 3.5](#)

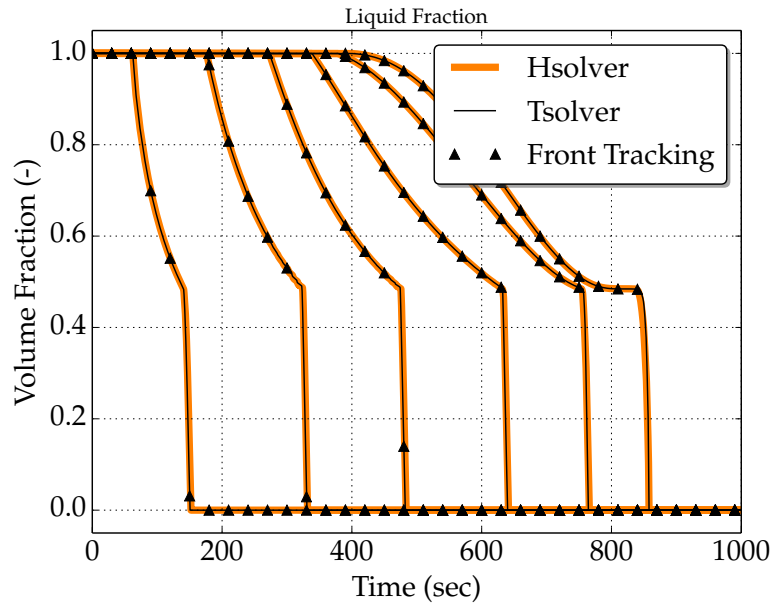
Parameter	Symbol	Value	Unit
Nominal composition	w_0	7	wt.%
Liquidus temperature	T_L	618	°C
Eutectic temperature	T_E	577	°C
Segregation coefficient	k	0.13	—
Liquidus slope	m_L	−6.5	K wt.% ^{−1}
Density	ρ	2600	kg m ^{−3}
Liquid heat capacity	C_p	1000	J kg ^{−1} K ^{−1}
Enthalpy of fusion	L	365 384	J kg ^{−1}
Thermal conductivity	κ	70	W m ^{−1} K ^{−1}
Heat transfer coefficient	h_{ext}	500	W m ^{−2} K ^{−1}
External temperature	T_{ext}	100	°C
Initial temperature	T_0	800	°C
Ingot length		0.1	m
FE mesh size		10 ^{−3}	m
Time step	Δt	0.1	s
Convergence criterion (residual)	ε_R	10 ^{−6}	—
Convergence criterion (temperature)	ε_T	10 ^{−2}	K

3.5 Application: multicomponent alloy solidification

We have shown that the efficiency of the temperature-based resolution resides in its performance when combined with thermodynamic tabulations. A multicomponent alloy consists of at least two solute elements, and therefore the tabulation size increases, hence the number of search operations also increases. To demonstrate the



(a)



(b)

Fig. 3.5 – Computed unidirectional heat diffusion during solidification of an Al-7 wt.% Si alloy using (orange) the enthalpy method and (black) the temperature method, comparison being made for (a) cooling curves and (b) the liquid fraction history. Each curve corresponds to a position along the sample, from 0 cm (cooling side) to 10 cm (insulated side), with 2 cm spacing between the positions. The reference solution by the Front Tracking method (values in shown by the triangular markers).

3.5. Application: multicomponent alloy solidification

speed-up ability of the temperature-based approach while predicting all phase transformations during macrosegregation caused solely by mass diffusion, we consider the solidification of a ternary alloy, Fe-2 wt.% C-30 wt.% Cr. In order to neglect fluid flow resolution, we assume that solidification in this case is so slow that no forces are generated inside the melt, while additionally all buoyancy forces are also neglected, so no momentum conservation is solved in this section.

As illustrated in [fig. 3.6a](#), the alloy domain has a cylinder shape close to 3-inch height \times 1-inch diameter. Exact values are reported in [table 3.3](#) with all material properties, initial and boundary conditions, as well as numerical parameters for the simulations. The steel melt is initially at 1395 °C. The temperature of the bottom surface is imposed with a constant decreasing rate of 0.1 K s⁻¹ starting with 1380 °C as shown in [fig. 3.6b](#), i.e. 40 °C higher than the nominal liquidus temperature as shown in [fig. 3.7](#). The other surfaces are kept adiabatic.

The cylinder is held in a vertical position parallel to the gravity vector, the latter pointing downwards. [fig. 3.7](#) also provides the transformation path of the alloy at nominal composition, i.e. assuming no macrosegregation and full thermodynamic equilibrium as computed with ThermoCalc and the TCFE6 database [[TCFE6 2010](#); [Andersson et al. 2002](#)]. A total of 5 phases need to be handled, the characteristic temperature for their formation being reported in [fig. 3.6b](#).

3.5.1 Tabulations

Full thermodynamic equilibrium is considered in the present case. Due to macrosegregation, the average composition is expected to continuously vary in time and space during casting. Transformation paths are thus determined a priori for a set of average compositions around the nominal value. Hence, carbon content varies in the interval [1.8 wt.%, 2.2 wt.%] while chromium content variation is in the interval [27 wt.%, 33 wt.%]. The offset of $\pm 10\%$ with respect to the nominal composition value allows tabulating relatively small composition steps to ensure a fairly accurate mapping when compared to the corresponding ternary phase diagram.

The average composition step is 0.04 wt.% for carbon and 0.6 wt.% for chromium, thus representing 2% intervals with respect to the nominal composition. The temperature varies in the interval [100 °C, 1600 °C] by 5 °C steps. For each triplet (carbon content in wt.% C, w_{C0} , chromium content in wt.% Cr, w_{Cr0} , temperature in K) corresponds a phase fraction g^ϕ and a pair of intrinsic phase composition ($\langle w_C \rangle^\phi, \langle w_{Cr} \rangle^\phi$), ϕ representing a phase. For the 5 phases listed in [fig. 3.7](#) (LIQ=liquid, BCC=ferrite, FCC=austenite, M_7C_3 =carbide, CEM=cementite), the enthalpy $\langle h \rangle^\phi$ and density $\langle \rho \rangle^\phi$, are tabulated as functions of temperature and phase intrinsic composition. If this lat-

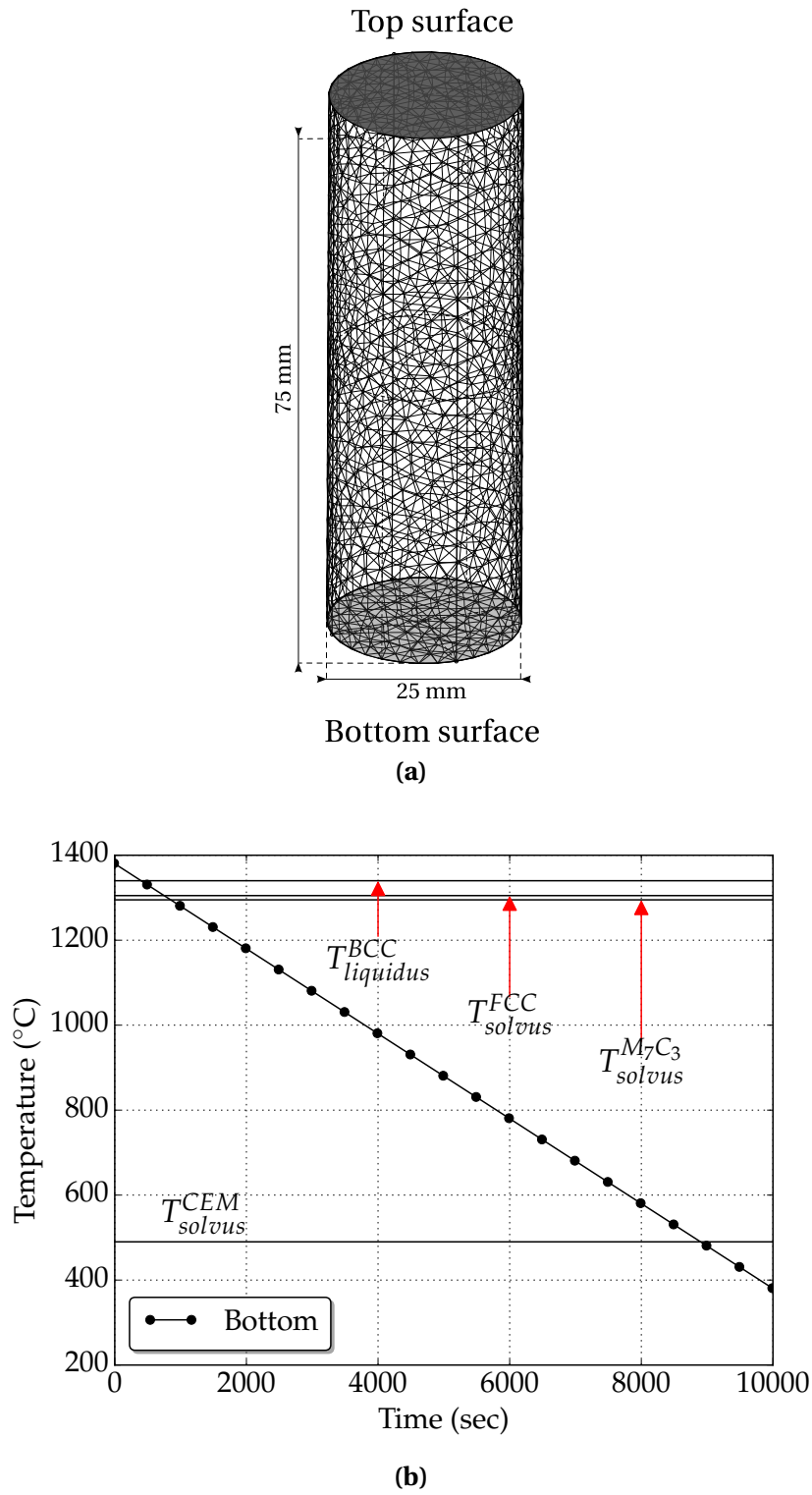


Fig. 3.6 – Configurations for upward directional casting of (a) a 1-inch diameter \times 3-inches height cylindrical domain for which (b) temperature-time conditions are imposed at its bottom surface.

3.5. Application: multicomponent alloy solidification

ter input lies between two tabulated values, a linear interpolation is performed to determine the output, i.e. phase enthalpy and density. With the advancement of solidification, the liquid is enriched or depleted with solute by macrosegregation, which enables new solidification paths. It means that the primary solidifying phase is not necessarily the same as when considering the nominal composition. For this reason, the tabulation approach is interesting inasmuch as it provides phase transformation paths and values of phase properties that are compatible with the system's actual composition.

Figure 3.8 summarises the tabulated thermodynamic data for two sets of average composition for the considered ternary system. Note that in the present test case, phase densities are taken constant ($\langle \rho \rangle^s = \langle \rho \rangle^l = 6725 \text{ kg m}^{-3}$). Therefore they are not tabulated. With this assumption, no shrinkage occurs upon phase change.

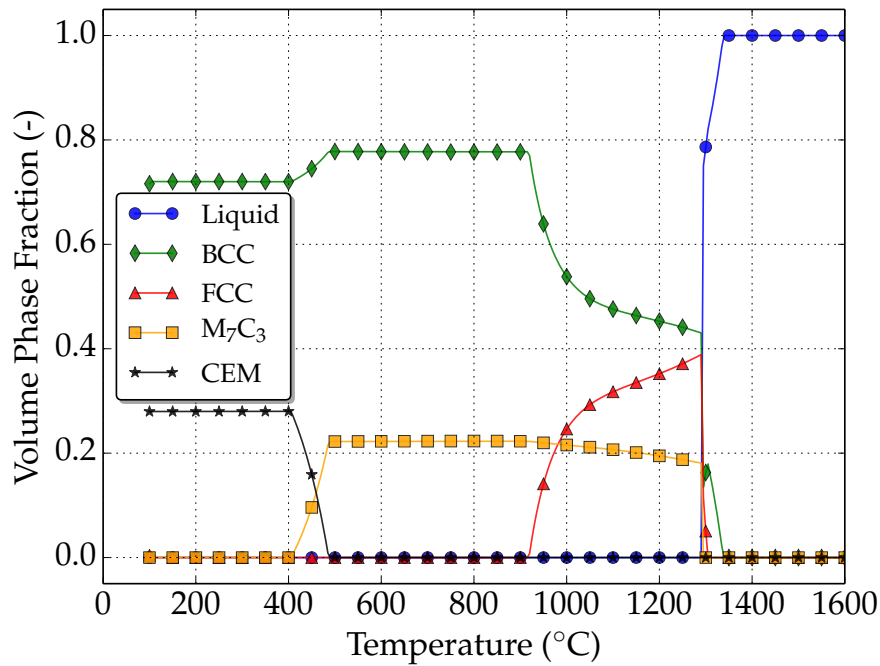


Fig. 3.7 – Thermodynamic mapping [TCFE6 2010; Andersson et al. 2002] of the transformation path for the Fe-2 wt.% C-30 wt.% Cr at nominal composition.

3.5.2 Discussion

A first case is considered without macrosegregation, that is, all mechanical driving forces are bypassed, leading to a static melt. This is achieved by nullifying the thermal and solutal expansion coefficients, which is equivalent to a constant density in space and time, i.e. no Boussinesq force is considered. This way, the average composition

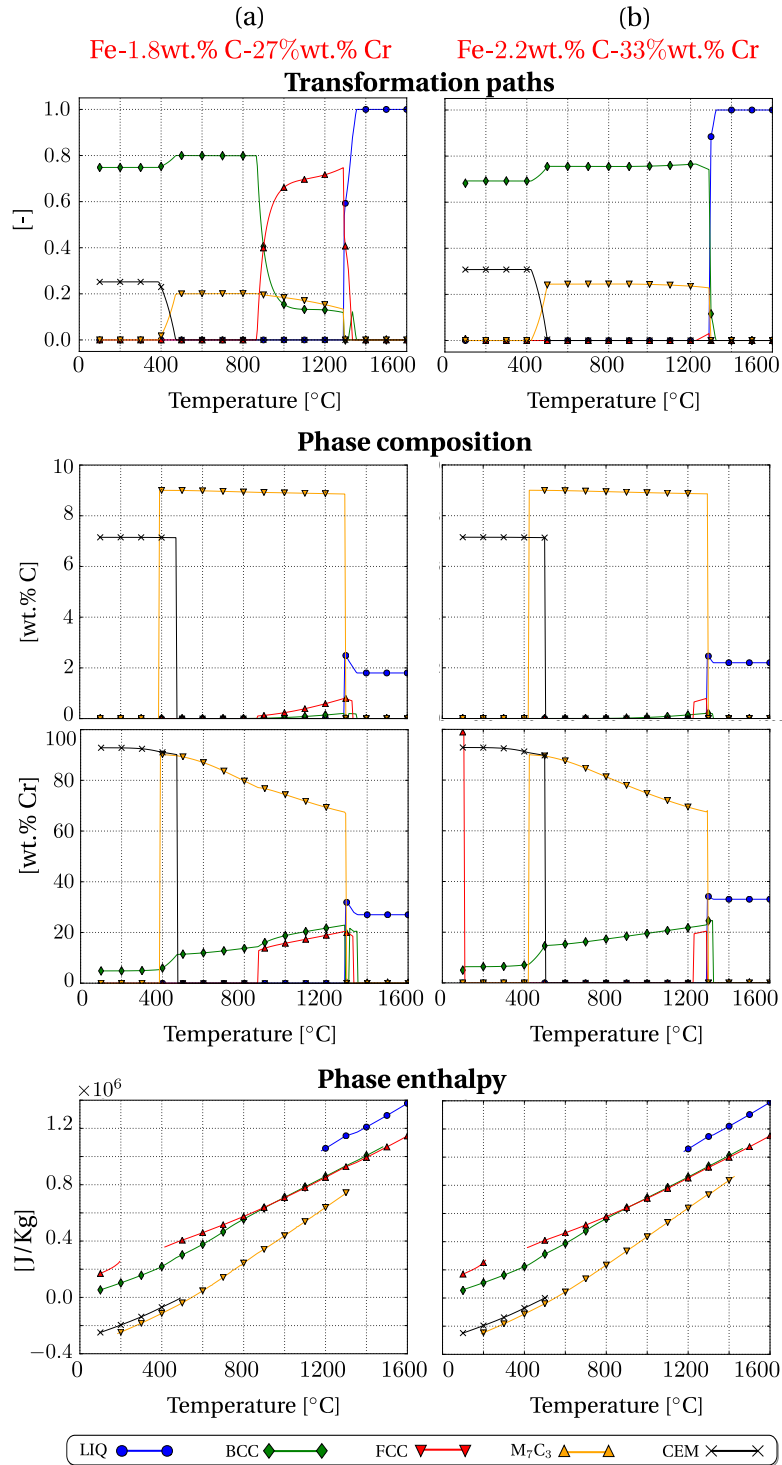


Fig. 3.8 – Tabulated thermodynamic data for the ternary system Fe-C-Cr alloy with software Thermo-Calc [Andersson et al. 2002] with database TCFE6 [TCFE6 2010]. The two columns represent two values of average composition, for a) low carbon and chromium content and b) high carbon and chromium content. The effect of their variation on transformation paths, phase compositions and phase enthalpies is shown in the corresponding graphs.

3.5. Application: multicomponent alloy solidification

may only vary due to diffusion in the liquid phase.

Diffusion is significantly small in the present case and can be neglected too. The composition distribution thus maintains a homogeneous aspect throughout the sample during the entire cooling sequence. The phase transformations then are necessarily expected to follow the unique path shown in [fig. 3.7](#). After 407 s of cooling, the liquidus isotherm enters the bottom surface of the geometry and starts its upward propagation, marking the solidification onset.

[Figure 3.9](#) presents the simulation results at 3 successive times for the distribution of the solute species and the temperature, as well as for the fraction of phases listed in [fig. 3.7](#). At 600 s, a fully liquid region is still largely present while the mushy zone is made of liquid plus the primary solid phase (ferrite). At 10 560 s, the sample is fully solid, with fractions of ferrite and cementite that corresponds to the values read in [fig. 3.7](#) at low temperature. At the selected intermediate time, the presence of 4 phases is found. The solid region at the bottom of the cylinder is made of ferrite, austenite plus carbide, the temperature being still too high to permit the cementite to form. The mushy zone above the solid region is characterized by the presence of 3 phases due to a peritectic reaction taking place that progressively transforms ferrite into austenite in the presence of liquid.

It can be noticed that the phase fraction isovalues in [fig. 3.9](#) (at 600 s) are horizontal, owing this to two factors: the first is the temperature field, which varies unidirectionally from bottom to top, controlled by thermal diffusion, while the second is the uniform average composition throughout the sample due to the absence of convection. In fact both factors are consequences of the flow absence, which would transport heat and solute by advection, thus inevitably changing the phase distribution. The succeeding phase change is a solid-state transformation where α -ferrite and the carbide M_7C_3 react to form cementite after cooling below 490 °C, as shown in [fig. 3.6b](#). The reaction is relatively slow, ending with 28% of cementite and 72% of α -ferrite.

Chapter 3. Energy balance with thermodynamic tabulations

Table 3.3 – Solidification parameters for the Fe-2 wt.% C-30 wt.% Cr alloy.

Parameter	Symbol	Value	Unit
Nominal composition	w_{C0}	2	wt. %
	w_{Cr0}	30	wt. %
Characteristic temperatures	T_{bottom}	fig. 3.6b	°C
Phase fraction	g^ϕ	Tabulations fig. 3.8	—
Phase enthalpy	$\langle h \rangle^\phi$	Tabulations fig. 3.8	—
Phase composition	$\langle w_C \rangle^\phi$	Tabulations fig. 3.8	wt. %
Phase composition	$\langle w_{Cr} \rangle^\phi$	Tabulations fig. 3.8	wt. %
Diffusion coefficients	$\langle D_C \rangle^l$	15×10^{-10}	$\text{m}^2 \text{s}^{-1}$
	$\langle D_{Cr} \rangle^l$	15×10^{-10}	$\text{m}^2 \text{s}^{-1}$
Dynamic viscosity	μ^l	2×10^{-3}	Pa s
Thermal expansion coefficient	β_T	8.96×10^{-5}	K^{-1}
Solutal expansion coefficient	$\beta_{\langle w_C \rangle^l}$	1.54×10^{-3}	wt. \%^{-1}
	$\beta_{\langle w_{Cr} \rangle^l}$	1.72×10^{-2}	wt. \%^{-1}
Thermal conductivity in the solid	$\langle \kappa \rangle^s$	40	$\text{W m}^{-1} \text{K}^{-1}$
Thermal conductivity in the liquid	$\langle \kappa \rangle^l$	28	$\text{W m}^{-1} \text{K}^{-1}$
Dendrite arm spacing	λ	60×10^{-6}	m
Density	ρ_0^l	6725	kg m^{-3}
Reference composition (carbon)	$\langle w_C \rangle_{\text{ref}}^l$	2	wt. %
Reference composition (chromium)	$\langle w_{Cr} \rangle_{\text{ref}}^l$	30	wt. %
Reference temperature	$\langle w_C \rangle_{\text{ref}}^l$	1377	°C
Initial temperature	T_0	1395	°C
Ingot diameter		25×10^{-3}	m
Ingot length		75×10^{-3}	m
FE mesh size		10^{-3}	m
Time step	Δt	0.1	s
Convergence criterion (residual)	ε_R	10^{-6}	—
Convergence criterion (temperature)	ε_T	10^{-2}	K

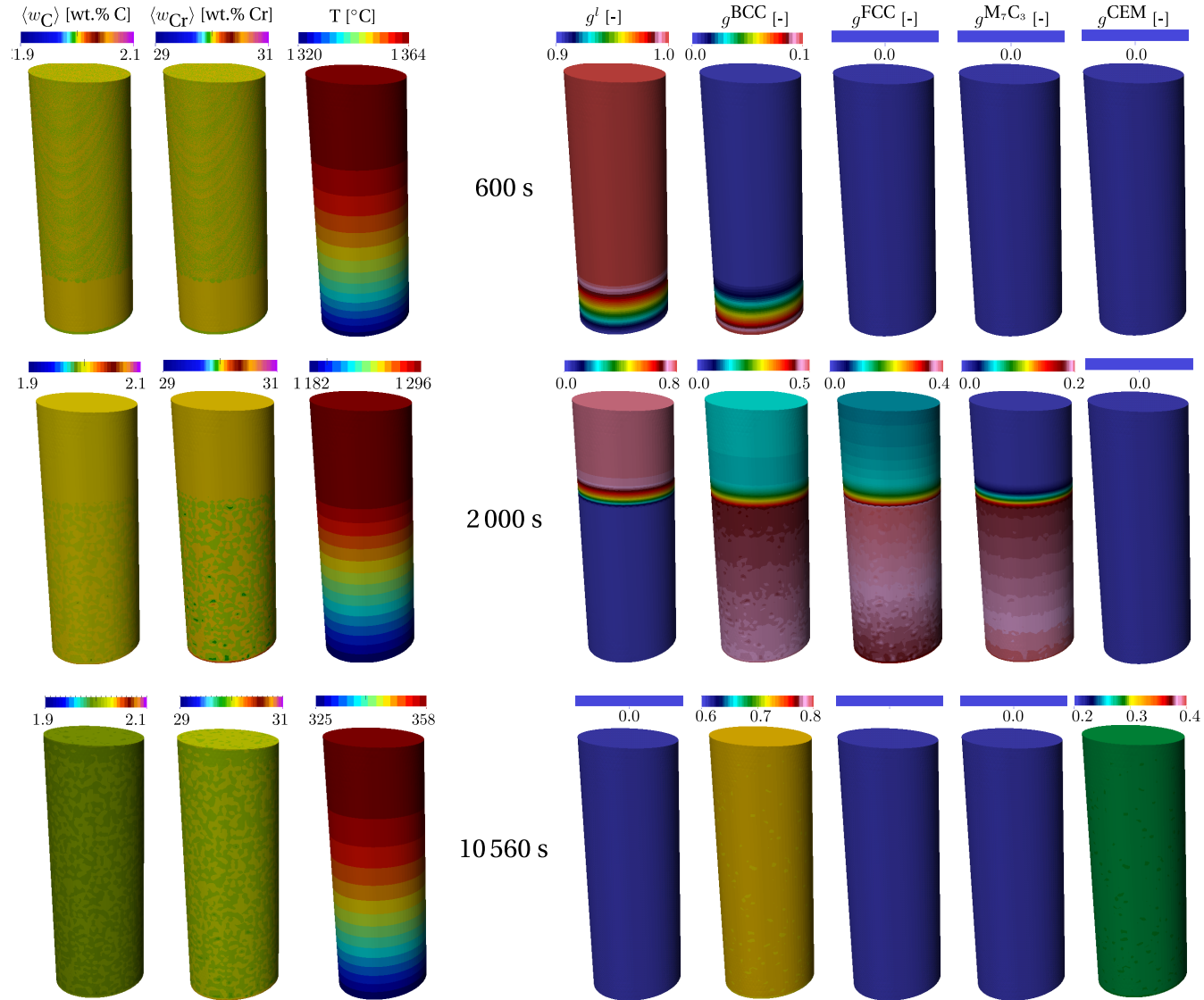


Fig. 3.9 – Upward solidification of a cylinder rod with a static liquid at 3 stages in a Fe-2 wt.% C-30 wt.% Cr. The left columns show the average composition and temperature distribution, while the right columns show the phase fractions.

3.6 Limitations

The *Tsolver* method is well suited for solidification problems with macrosegregation. In this chapter, only pure diffusion cases were simulated. The next chapter discusses the details of solving Navier-Stokes equations while predicting macrosegregation, showing thus the advantage of using the thermodynamic tabulation approach with the *Tsolver*. However, some limitations are still present and need to be explained.

First, we address the technical difficulties inherent to the solver. The previously shown algorithm in [fig. 3.4](#), showed that the Newton-Raphson method is used to linearise the energy equation then iterate on the value of the nonlinear $\frac{\partial H}{\partial T}$ term. The initial value of this term is crucial to achieve a good convergence rate, and therefore it is only manually set equal to initial phases volume heat capacity. This should evolve into an automatic initialisation based on a first evaluation given by the tabulation, making the approach more general.

The second point is the number of iterations needed by the method to converge. Although the Newton-Raphson algorithm is known for its quadratic convergence speed, imposing low convergence thresholds ([eq. \(3.25\)](#)) may easily raise the number of iterations to an average of 5 iterations before convergence can be achieved. In situations without phase change but only variable slope of enthalpy versus temperature, from 1 to 2 iterations are needed to converge. A possible solution is to implement a line search method which is called at each iteration, whenever the residual of the nonlinear system increases instead of steadily decreasing.

Regarding the thermodynamic tabulations, they are only obtained by assuming full equilibrium for macrosegregation calculations. For many binary alloys, little differences are usually seen when the macrosegregation is induced by a full equilibrium and a non equilibrium solidification. It is clear however that this approximation remains limiting for multicomponent alloys. For steels, a third type of approximation is even required, named partial equilibrium, that considers equal chemical potential of interstitial elements in all phases (e.g., C), while substitutional species in the solid phases (e.g., Cr) are frozen [[Koshikawa et al. 2014](#)].

Résumé chapitre 3

Ce chapitre reprend les détails du solveur pour la conservation d'énergie avec changement de phase utilisé au CEMEF. Celui-ci est basé sur une méthode enthalpique, dénommée *Hsolver*, dont la variable principale est l'enthalpie moyenne volumique du système, $\langle \rho h \rangle$. Ce solveur est aussi compatible avec des données tabulées provenant de bases de données thermodynamiques, fournissant des valeurs précises pour chaque phase ϕ présente au moment de la transformation : fraction g^ϕ , composition intrinsèque $\langle w_i \rangle^\phi$, enthalpie massique $\langle h \rangle^\phi$ et densité $\langle \rho \rangle^\phi$. Avec ces données, l'équation de conservation de l'énergie est résolue dans son état nonlinéaire provenant de la dépendance de ρh par rapport aux propriétés citées précédemment, sachant que celles-ci varient aussi en fonction de la composition moyenne du volume élémentaire représentatif.

Cependant, la résolution *Hsolver* nécessite une lourde recherche itérative à chaque pas de temps, consistant à convertir $\langle \rho h \rangle$ en température T pour évaluer le résidu du système nonlinéaire. Cette conversion est dénommée *H2T* et elle est compliquée du fait que les bases thermodynamiques fournissent la température comme donnée d'entrée, ce qui nous oblige de faire la recherche inverse itérative.

Dans ce chapitre, on propose de remplacer la conversion *H2T* par une autre, *T2H*. Comme son nom l'indique, on part de l'idée que la température soit la variable principale du système et on devrait alors trouver l'enthalpie moyenne volumique à chaque pas de temps. Avec ce changement, on propose donc une nouvelle formulation éléments finis, *Tsolver*, mettant en évidence les principales différences algorithmiques des deux résolutions.

Nous validons la formulation *Tsolver* dans un cas purement diffusif et comparé à des calculs faits avec la méthode *Hsolver*, ainsi qu'une comparaison avec une solution numérique obtenue par une méthode de suivi de front [GANDIN 2000]. Ensuite, nous montrons une application de solidification dirigée d'un système ternaire, Fe-0.2 wt.% C-30 wt.% Cr, en régime diffusif. Enfin, les limitations et les voies d'évolutions de la méthode *Tsolver* avec les tabulations sont détaillées.

Bibliography

[Andersson et al. 2002]

Andersson, J.-O., Helander, T., Höglund, L., Shi, P., and Sundman, B. (2002). “Thermo-Calc & DICTRA, computational tools for materials science”. *Calphad*, 26 (2), pp. 273–312. URL: <http://www.sciencedirect.com/science/article/pii/S0364591602000378> (cited on pages 63, 65, 66).

[Bellet et al. 2009]

Bellet, M., Combeau, H., Fautrelle, Y., Gobin, D., Rady, M., Arquis, E., Budenkova, O., Dussoubs, B., Duterrail, Y., Kumar, A., Gandin, C. A., Goyeau, B., Mosbah, S., and Založnik, M. (2009). “Call for contributions to a numerical benchmark problem for 2D columnar solidification of binary alloys”. *International Journal of Thermal Sciences*, 48 (11), pp. 2013–2016. URL: <http://www.sciencedirect.com/science/article/pii/S129007290900177X> (cited on page 48).

[Carozzani et al. 2013]

Carozzani, T., Gandin, C.-A., Digonnet, H., Bellet, M., Zaidat, K., and Fautrelle, Y. (2013). “Direct Simulation of a Solidification Benchmark Experiment”. *Metallurgical and Materials Transactions A*, 44 (2), pp. 873–887. URL: <http://link.springer.com/article/10.1007/s11661-012-1465-1> (cited on page 48).

[Doré et al. 2000]

Doré, X., Combeau, H., and Rappaz, M. (2000). “Modelling of microsegregation in ternary alloys: Application to the solidification of Al–Mg–Si”. *Acta Materialia*, 48 (15), pp. 3951–3962. URL: <http://www.sciencedirect.com/science/article/pii/S1359645400001774> (cited on page 48).

[Du et al. 2007]

Du, Q., Eskin, D. G., and Katgerman, L. (2007). “Modeling Macrosegregation during Direct-Chill Casting of Multicomponent Aluminum Alloys”. *Metallurgical and Materials Transactions A*, 38 (1), pp. 180–189. URL: <http://link.springer.com/article/10.1007/s11661-006-9042-0> (cited on page 48).

[Gandin 2000]

Gandin, C. A. (2000). “From constrained to unconstrained growth during directional solidification”. *Acta Materialia*, 48 (10), pp. 2483–2501. URL: <http://www.sciencedirect.com/science/article/pii/S1359645400000707> (cited on pages 58, 71).

[Koshikawa et al. 2014]

Koshikawa, T., Gandin, C.-A., Bellet, M., Yamamura, H., and Bobadilla, M. (2014). “Computation of Phase Transformation Paths in Steels by a Combination of the Partial- and Para-equilibrium Thermodynamic Approximations”. *ISIJ International*, 54 (6), pp. 1274–1282 (cited on page 70).

Bibliography

[Rappaz et al. 2003]

Rappaz, M., Bellet, M., and Deville, M. (2003). *Numerical Modeling in Materials Science and Engineering*. Springer Series in Computational Mathematics. Springer Berlin Heidelberg (cited on pages 49, 54).

[Süli 2000]

Süli, E. (2000). *Lecture Notes on Finite Element Methods for Partial Differential Equations* (cited on page 52).

[Swaminathan and Voller 1993]

Swaminathan, C. R. and Voller, V. R. (1993). "On The Enthalpy Method". *International Journal of Numerical Methods for Heat & Fluid Flow*, 3 (3), pp. 233–244. URL: <http://www.emeraldinsight.com/journals.htm?articleid=1665561&show=abstract> (cited on page 48).

[TCFE6 2010]

TCFE6 (2010). *TCFE6: a thermodynamic database for different kinds of steels and Fe-based alloys*. Stockholm, SE. URL: <http://goo.gl/qiD3kE> (cited on pages 63, 65, 66).

[Thuinet and Combeau 2004]

Thuinet, L. and Combeau, H. (2004). "Prediction of macrosegregation during the solidification involving a peritectic transformation for multicomponent steels". *Journal of Materials Science*, 39 (24), pp. 7213–7219. URL: <http://link.springer.com/article/10.1023/B%3AJMSC.0000048734.34597.1e> (cited on page 48).

Modélisation par Level Set des macroségrégations induites par le retrait à la solidification

RESUME : La macroségrégation est un défaut connu dans les procédés de coulées industrielles. La genèse de ce défaut est la conséquence de l'interaction complexe entre la microségrégation ou la distribution des espèces chimiques à l'échelle de la microstructure et les mouvements des phases liquide et solides. Les hétérogénéités de concentration en solutés à l'échelle de la pièce peuvent être rédhibitoires vis-à-vis de la qualité du produit. Dans ce travail, on propose un modèle numérique pour simuler et prédire la formation des macroségrégations en coeur des pièces d'alliages multi-constitués, induites par des variations thermiques et solutales dans la phase liquide. Dans un premier temps, on considère que le métal solidifie à volume constant. Dans ce contexte, la convection thermosolutale est étudiée ainsi que son influence sur la formation des canaux ségrégés à différentes échelles de modélisation. Dans un deuxième temps, le modèle vise à prédire les macroségrégations en présence de changement de volume du métal, dont la cause principale est le retrait à la solidification, pouvant être à l'origine du phénomène de ségrégation inverse. La surface entre le métal et le gaz environnant au cours du retrait évolue pendant le retrait en fonction du chemin de solidification qui varie avec la macroségrégation. Cette évolution d'interface est suivie par la méthode Level set. Des prédictions de concentration moyenne, couplées aux bases de données thermodynamiques pour mieux prédire les chemins de solidification des alliages multi-constitués, sont analysées et comparées avec des résultats expérimentaux. Finalement, des calculs de solidification en microgravité sont présentées, simulant un essai expérimental dans le contexte du projet CCEMLCC lancé par l'Agence Spatiale Européenne. Les résultats en fin de solidification montrent un accord acceptable quant à la forme et l'élongation des échantillons solidifiés. Ces calculs sont faits avec des approximations binaire, ternaire et quaternaire d'une même nuance d'acier utilisée dans les essais en microgravité.

Mots clés : modélisation, solidification, ségrégation, Level Set, éléments finis, métallurgie

Numerical modeling of macrosegregation formed during solidification with shrinkage using a Level Set Approach

ABSTRACT : Macrosegregation is key defect in industrial casting processes. During solidification, solute redistribution at the scale of microstructure, also known as microsegregation, take place with complex interactions, in order to form one or more solid phases. These interactions between microsegregation and movements of liquid and solid phases may lead to macrosegregations. These solute heterogeneities spanning on a larger scale, may result in a bad casting quality. In this thesis, we propose a numerical model to simulate and predict macrosegregations occurring in the centre of multicomponent alloys, caused by thermal and solutal variations in the liquid phase. First, we assume that the metallic alloy solidifies with a constant volume. In this context, we study the influence of thermosolutal convection on the formation of channel segregations, at different modelling scales. The second part of this modelling work consider solidification while the metallic alloy's volume is decreasing, mainly due to overall density variation, also known as solidification shrinkage, possibly leading to the so-called inverse segregation phenomenon, appearing on the alloy's skin. In the context of solidification shrinkage, the shape of the metal's boundary with surrounding gases varies according to a constantly changing solidification path due to macrosegregation. The Level Set method is therefore used to track its evolution with time. Composition predictions, coupled with thermodynamic database mappings for more accurate multicomponent solidification paths, are analysed and compared to existing experimental setups. Finally, simulations of a reduced-gravity solidification cases are performed, mocking an experimental benchmark from the CCEMLCC project launched by the European Space Agency. The results show acceptable agreement for the final shape, compared to experimental results. These computations were performed with binary, ternary and quaternary approximations of the same steel grade which was used in reduced-gravity experiments.

Keywords : modelling, solidification, segregation, Level Set, finite elements, metallurgy

